Environ Fluid Mech
DOI 10.1007/s10652-013-9315-2

ORIGINAL ARTICLE

Dynamics of the head of gravity currents

Helena I. S. Nogueira · Claudia Adduce · Elsa Alves · Mário J. Franca

Received: 8 January 2013 / Accepted: 23 September 2013

Abstract The present work experimentally investigates the dynamics of unsteady gravity currents produced by lock-release of a saline mixture into a fresh water tank. Seven different experimental runs were performed by varying the density of the saline mixture in the lock and the bed roughness. Experiments were conducted in a Perspex flume, of horizontal bed and rectangular cross section, and recorded with a CCD camera. An image analysis technique was applied to visualize and characterize the current allowing thus the understanding of its general dynamics and, more specifically, of the current head dynamics. The temporal evolution of both head length and mass shows repeated stretching and breaking cycles: during the stretching phase, the head length and mass grow until reaching a limit, then the head becomes unstable and breaks. In the instants of break, the head aspect ratio shows a limit of 0.2 and the mass of

H. I. S. Nogueira (✉)
Department of Civil Engineering and IMAR-CMA, University of Coimbra,
Coimbra, Portugal
e-mail: hnogueira@dec.uc.pt

C. Adduce
Department of Civil Engineering, University of Rome, "Roma Tre", Rome, Italy
e-mail: claudia.adduce@uniroma3.it

E. Alves
Department of Hydraulics and Environment, National Laboratory of Civil Engineering,
Lisbon, Portugal
e-mail: ealves@lnec.pt

M. J. Franca
Department of Civil Engineering and IMAR-CMA, New University of Lisbon,
Lisbon, Portugal
e-mail: mfranca@fct.unl.pt

Present address:
M. J. Franca
Laboratoire de Constructions Hydrauliques, École Polytechnique Fédérale de Lausanne,
Lausanne, Switzerland
e-mail: mario.franca@epfl.ch

Published online: 10 October 2013

the head is of the order of the initial mass in the lock. The average period of the herein called breaking events is seen to increase with bed roughness and the spatial periodicity of these events is seen to be approximately constant between runs. The rate of growth of the mass at the head is taken as a measure to assess entrainment and it is observed to occur at all stages of the current development. Entrainment rate at the head decreases in time suggesting this as a phenomenon ruled by local buoyancy and the similarity between runs shows independence from the initial reduced gravity and bed roughness.

Keywords Gravity currents · Head dynamics · Lock-exchange · Image analysis technique · Entrainment

1 Introduction

Gravity or density currents are buoyancy driven flows which can occur spontaneously in nature or resulting from human intervention. Examples of gravity currents in the atmosphere are katabatic winds, flows developing downslope originated by radiational cooling of air on the top of a mountain, sea-breeze fronts, driven by differences in temperature between two air masses, and avalanches of airborne snow and sand storms, where suspended particles play a major role in density gradients. In the water masses one may refer oceanic fronts, resulting from differences in temperature and salinity, and turbidity currents caused by high concentration of suspended particles. Several more examples can be found comprehensively in Simpson [56].

Gravity currents are pertinent to engineering sciences, namely in what concerns industrial safety and environmental protection. The release of pollutants into rivers, oil spillage in the ocean and desalination plant outflows are a few examples of anthropogenic gravity currents frequently with negative environmental impacts. The loss of storage in reservoirs, related to deposition of fine sediments due to turbidity currents, is a subject of great concern to hydraulic engineers and still a topic of research nowadays [7,32,43].

Gravity currents have been widely studied in laboratory through both continuous ([12,15,20,22,23,48] among many others) and instantaneous [2,25,29,36] releases of a heavier fluid into other fluid of lower density. Unsteady gravity currents experiments are usually performed through the lock-exchange technique [6,26,29,53,63], which consists in the release of a fixed volume of dense fluid into a lower density fluid. The differences in hydrostatic pressure between contacting fluids cause the denser fluid to flow along the bottom of the tank, while the lighter fluid flows along the top boundary, in the opposite direction. The development of gravity currents is typically an unsteady phenomenon, i.e., current kinematics and the inner density distribution are time varying, therefore the lock-exchange setup is a simple and convenient way to investigating the flow features of these particular currents. Numerical modeling has also been used to investigate the evolution and impact of gravity currents [2,10,13,23,27,33–35,44,47,59]. Although the motion of these currents is invariably three-dimensional, laboratory experiments and numerical results indicate that the large-scale features may be reasonably well described through a two-dimensional approach [27].

The dynamics of the head of gravity currents has been studied extensively, both experimentally and theoretically, since the second half of the XX century [5,12,55,57]. The three-dimensional behavior of the advancing head is related to two dominant modes of instability which govern the mixing processes: (i) Kelvin–Helmholtz instability, in which billows are generated at the head, induced by the opposite movement of contacting layers with different

densities, breaking at the rear of the head causing ambient fluid to be entrained; and (ii) lobes and clefts [55], generated by a convective instability formed at the foremost region of the head due to the incorporation of less dense fluid by the current head during its propagation along a no-slip lower boundary. Based on steady state experiments and using the shadowgraph technique to visualize the flow, [12] presented a model for the structure of the flow in the head region of a stationary current where three distinct layers are identified: a lower layer of undiluted dense fluid, an upper layer of ambient fluid and the layer in between, where mixing takes place. Hallworth et al. [26] and Hacker et al. [25] investigated unsteady gravity currents over horizontal beds produced by the lock-exchange technique and, through two different visualization techniques, commented the inner structure of the current. Hallworth et al. [26] observed that unsteady gravity currents have a distinct inner structure when compared to steady gravity currents, namely in what regards the extent of mixing: steady currents have a shorter mixing layer, near the upper boundary, above an undiluted layer which is continuously replenished by denser fluid from the tail. This model is, in its essence, similar to the three-layer model proposed earlier by Britter and Simpson [12]. Regarding entrainment into the head region, Hallworth et al. [26] argue that during the slumping phase the head remains undiluted, i.e., no entrainment takes place during this phase, and the head is progressively reduced in length. Thereafter, when the reflected bore reaches the current front, even though ambient fluid is continuously entrained into the head region, the head volume decreases as the current develops towards downstream due to mixed fluid left behind in the tail. Hacker et al. [25], through an image analysis technique based on light absorption, assess the density distribution within the current and show that this is more complex than what was previously accepted. By analyzing the temporal evolution of different iso-density contours, they observed that entrainment is present at all stages of the current development. The change of the aspect ratio of the lock, the gate removal and the Reynolds number of the flow were seen to influence the initial development of the current, leading to a broad range of density distribution within the current, originating different extents of mixing.

The general characteristics of gravity currents, such as density and location, are important in many applications in geophysics and civil engineering and are determined by the amount of entrained fluid into the current during its evolution. Ellison and Turner [20] drew attention to the entrainment phenomenon and performed experiments of continuously fed gravity currents over smooth bed with varying slope, with $Re \sim 1,000$. The entrainment parameter is therein defined as the ratio between the velocity of entrained fluid into the current and a velocity scale of the current (E) and it is shown to be dependent on bulk Richardson number. Based on their experiments, the well-known relation $E = (0.08 - 0.1Ri)/(1 + 5Ri)$ was established, valid for $Ri \leq 0.8$. They predict the entrainment parameter to be negligible for high Richardson numbers ($Ri > 0.8$). Their work motivated the development of further research on mixing in gravity currents ([17,16,22,26,48,52] among many others), being the parameterization of mixing in dense currents still an area of active research nowadays. The influence of Richardson number, or densimetric Froude number, on the entrainment parameter, as well as the slope of the bed, have been considered since the early works. Only recently, the dependence on Reynolds number was also investigated and seen to be fundamental in the prediction of entrainment [15,21,52], especially in natural flows with high Reynolds numbers ($Re \sim 10^7$) where results deviate substantially from the laboratory-based entrainment laws, usually obtained for $Re \sim 1,000$. In Adduce et al. [2] a two-layer shallow water model with entrainment was developed and tested by laboratory experiments with lock-exchange gravity currents in which both initial density and initial saline volume in the lock were varied. The entrainment was found to play a key role in the simulations.

Several laboratory studies have been based on image analysis techniques to investigate the dynamics of gravity currents [2,25,33,34,36,54] the last two with the very same apparatus herein used). Recent advances in measurement techniques have enabled velocity and density measurements within gravity currents. Particle Image Velocimetry and Particle-Tracking Velocimetry have been used to investigate the inner velocity field of the current [3,58,63] and the combination of PIV with such other methods, as Laser-Induced Fluorescence [37,49] and PIV-Scalar [23], allows the measurement of velocity and density simultaneously.

Most of the investigation efforts concern flows developing over smooth beds, though a few investigators have studied the effect of bed roughness in the dynamics of gravity currents. Peters and Venart [50] used Laser-Induced Fluorescence to investigate flow dynamics and mixing processes at the head region of continuously fed gravity currents developing over rough surfaces. They used regular square cross-section elements to produce bed roughness, spanning the full channel width, with four different side dimensions. In general, they observed that roughness decreases the front velocity and induces higher dilution in the head region. According to these authors, those effects are due to two mechanisms: an increase in the scale of the bed roughness inducing extra bed shear stress, thus extra flow resistance and consequent anticipation of the viscous effects; secondly, ambient fluid entrapped within the roughness layer is entrained into the current, contributing to a reduction of the buoyancy differences between current and ambient fluid which constitutes the flow driving force. Adduce et al. [1], with the very same apparatus herein used, performed experiments with rough bed using quartz sand. They used an image analysis technique to investigate the temporal evolution of the current and corroborated the findings reported in Peters and Venart [50] regarding roughness effects on front velocity reduction. Recently, Nogueira et al. [41] have confirmed that lock-released gravity currents over horizontal rough beds have a front velocity reduction, only noticeable during the inertial phase of development; during the slumping phase the front velocity is kept fairly constant, with values in the range obtained for smooth bed currents. The transition between the slumping and inertial phases was seen to occur earlier in the run where the highest bed roughness was used, which leads to the conclusion that the porosity and the scale of the roughness elements play a role in the kinematics of the current. The effect of bed roughness in gravity currents was numerically investigated by Özgökmen and Fischer [45]. The results of their simulations suggest that roughness increases drag, with effects on the velocity field, and mixing between the current and ambient fluid, modifying the density distribution within the current. Despite previous contributions, the effect of the bed roughness in the kinematics and in the mixing processes of gravity currents is yet far from being completely explored.

The present work aims at investigating the dynamics of the head of gravity currents, namely the influence of the density of the fluid in the lock and the bed roughness on entrainment of ambient fluid into the current. This research is based on an experimental work where lock-exchange density currents, induced by salinity differences, are reproduced under controlled conditions in an open tank. The development of the saline currents is captured by a CCD camera, using dye concentration as a tracer, allowing the reconstruction of time and space (2D) evolution of the density fields. Preliminary results of the experiments presented herein, regarding head dynamics over smooth and rough beds, were already presented in Nogueira et al. [40].

After this introduction, experimental details are given in Sect. 2, main results concerning head dynamics and entrainment are presented and discussed in Sect. 3, being Sect. 4 devoted to the main conclusions.

2 Experimental details

2.1 Facilities and experimental procedure

The lock-release experiments were performed in a horizontal and rectangular cross-section tank 3.0 m long, 0.2 m wide and 0.3 m deep (Fig. 1), with transparent Perspex walls at the Hydraulics Laboratory of University Roma Tre. The saline mixture with initial density ρ_1 is placed in a lock with a vertical sliding gate at a distance $x_0 = 0.15$ m from the upstream section, i.e. left wall, of the tank. The right side of the tank is filled with fresh water with density ρ_0, both sides filled up at same depth. In all experiments, the relative depth of the initial configuration is kept $h_0/H = 1$, where $h_0 = 0.20$ m is the depth of the fluid in the lock and H is the total depth of the ambient fluid.

Temperature measurements are performed in both fresh water in the tank and saline mixture in the lock. The kinematic viscosity of the saline mixture, ν, is a function of temperature, pressure and concentration of salt and is herein obtained through the results presented in Kestin et al. [30]. Densities of the saline mixture and of the ambient fluid are determined at the beginning of each run. A pycnometer is used to measure the density of the saline mixture, being the error of the weighing apparatus 0.05%. A controlled quantity of white colorant (E171, titanium dioxide) is added to the mixture in the lock to provide flow visualization.

The experiment starts when the gate is suddenly removed leading to the collapse of the vertical column of heavier fluid, forming a gravity current developing along the tank bed, while a current formed by ambient fluid develops above the denser current in the opposite direction. During this process, mixing between both currents takes place, inducing entrainment of ambient fluid into the heavier density current, reducing its density. The experiment ends when the current reaches the right end wall of the tank.

The evolution of the gravity current is recorded by a CCD camera with 768 × 576 pixels of resolution and acquisition frequency of 25 Hz. The captured video frames are subsequently converted into gray scale matrices in the region of the tank with fluid (702 × 43 pixels) and then converted into instantaneous density fields of the current through a calibration procedure. Results are shown for a selected window of the field of view (dashed rectangle in Fig. 1). The evaluation of the current density distribution was based on a relation between reflected light intensity and concentration of dye present in the flow; this latter is considered linearly correlated with the salt concentration within the current body. A calibration procedure was carried out for each single pixel in the region defined earlier to establish the relation between the amount of dye in the water and the values of gray scale in the frames representing light

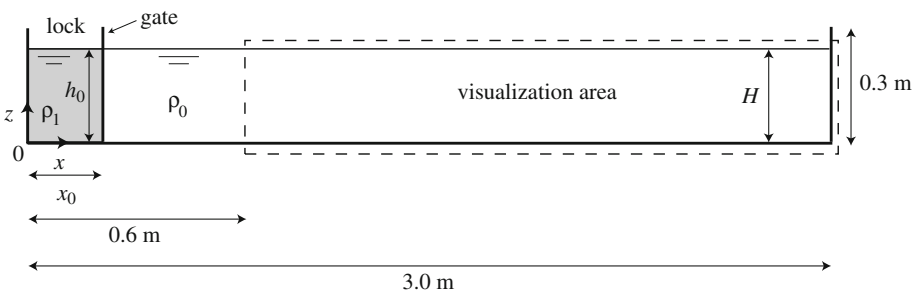

Fig. 1 Schematic view of the Perspex tank used for the lock-exchange experiments with main dimensions and the Cartesian reference system considered

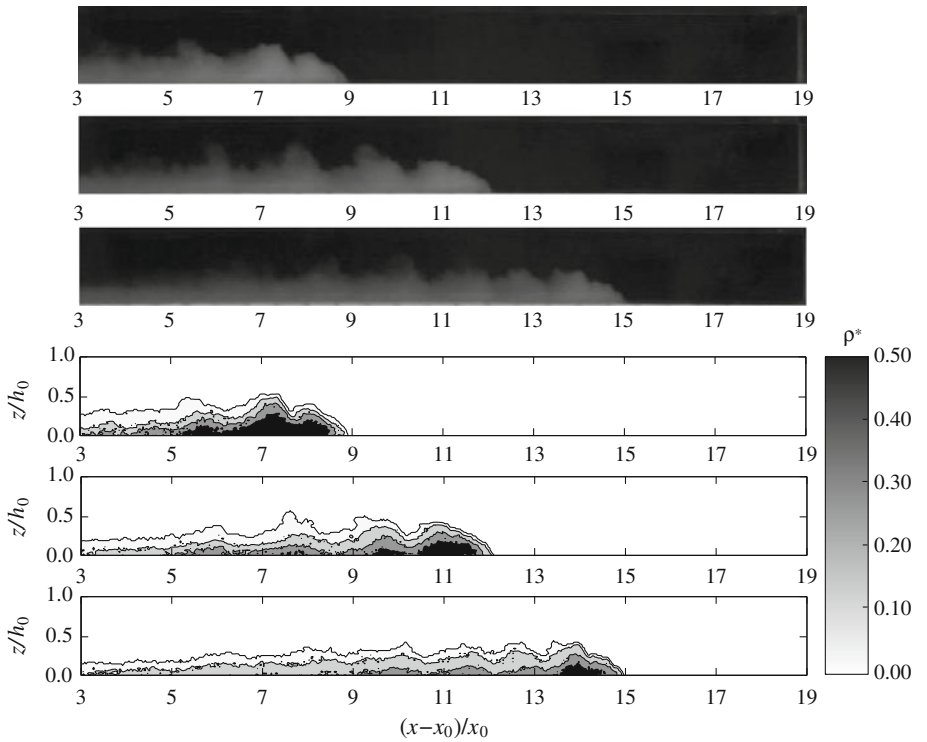

Fig. 2 (*top*) Pictures of the current acquired at $t = 20$, 28 and 36 s after the gate removal in run D1; (*bottom*) corresponding non-dimensional iso-density contours plotted for $\rho^* = 0.02$, 0.15, 0.30 and 0.50

intensities. The results from this procedure are then verified and eventually corrected through total salt mass conservation principle applied to the entire experimental tank, taking into account the current mass and the mass of ambient fluid. Further details on the experimental technique and calibration procedure can be found in Nogueira et al. [42].

The conversion of gray scale video images in density fields is illustrated in Fig. 2 which shows pictures of the current acquired at t = 20, 28 and 36 s, t being the time after the gate removal, in run D1 (experimental runs defined in Table 1) and the corresponding reconstructed non-dimensional iso-density contours plotted for 0.02, 0.15, 0.30 and 0.50. The instantaneous non-dimensional density is defined as $\rho^*(x, z, t) = (\rho(x, z, t) - \rho_0)/(\rho_1 - \rho_0)$, where $\rho(x, z, t)$ is the local density of the current. The non-dimensional iso-density contour of 0.02 was adopted as the boundary of the current in the analysis presented further in the text.

2.2 Experiments description

Seven lock-exchange experiments were performed varying the initial density of the saline mixture in the lock, ρ_1, and the bed roughness, k_s, leading to two different types of runs, identified by D and R, respectively. The experiments were performed by varying one parameter at a time. Table 1 summarizes the parameters of the experiments and the symbols used further in the text. Each run was performed for an initial reduced gravity of the mixture in the lock, defined as

Table 1 Main parameters of the experimental runs

Run	ρ_0 (kg m^{-3})	ρ_1 (kg m^{-3})	h_0/x_0	k_s (mm)	g'_0 (m s^{-2})	u_0 (m s^{-1})	$u_{f,b}$ (m s^{-1})	Δu (m s^{-1})	Re_0	Re_b	Fr_b	Symbols in figures
D1	997.8	1,014.7	1.33	0.0	0.17	0.18	0.06	0.09	40,756	3,872	0.76	∘
D2	997.4	1,029.7	1.33	0.0	0.32	0.25	0.09	0.13	53,230	5,716	0.78	□
D3	997.4	1,044.6	1.33	0.0	0.46	0.30	0.11	0.16	66,918	7,237	0.83	△
D4	998.0	1,060.0	1.33	0.0	0.61	0.35	0.12	0.19	64,680	8,244	0.83	▽
R1	997.4	1,030.0	1.33	2.9	0.32	0.25	0.08	0.13	64,922	5,647	0.80	+
R2	997.4	1,030.1	1.33	4.6	0.32	0.25	0.08	0.12	55,058	5,283	0.75	×
R3	997.6	1,030.2	1.33	24.6	0.32	0.25	0.07	0.10	52,479	4,385	0.59	∗

$$g'_0 = g\frac{\rho_1 - \rho_0}{\rho_0} \tag{1}$$

being g the acceleration due to gravity. Main parameters are presented in the non-dimensional form by adopting the following dimensionally independent scales, in accordance with previous studies [25,36,60], namely lock length x_0 (cf. Fig. 1) as length scale and a velocity scale given by the buoyancy velocity defined as

$$u_0 = \sqrt{g'_0 h_0} \tag{2}$$

As shown in Table 1, the Reynolds number based on bulk initial quantities, $Re_0 = u_0 h_0/\nu$, is greater than 40000, reflecting the turbulent nature of the gravity currents performed in this study.

The rough bed in the R-type experiments was made by placing a thick layer of sediments, mainly constituted by quartz and feldspar. The sediment disposal in the tank was made in order to create a layer with thickness of around $3D_{50}$, where D_{50} is the grain size diameter for which 50% of the amount of sediments have smaller diameters; herein D_{50} was taken as the roughness scale k_s (Table 1). The tank was leveled horizontally and the grains were set uniformly throughout the tank, where no bed forms were allowed. Further details can be found in Nogueira et al. [41].

Additionally, in Table 1 are presented the bulk front velocity of the dense current, $u_{f,b}$, obtained by taking the initial and final positions of the current front and the duration of the experiment; the difference between mean front velocities of both denser and return currents, Δu; and the bulk values of the Reynolds and Froude numbers, Re_b and Fr_b, respectively, explained further in Sect. 3.1.

3 Results

3.1 Entrainment parameterization

Following previous definitions for a bulk entrainment parameter [20], this was herein estimated by:

$$E_b = \frac{u_e}{u}, \tag{3}$$

being u_e the entrainment velocity and u a characteristic velocity of the flow, usually taken as the current velocity relative to its surroundings. The entrainment velocity is obtained by the entrained discharge per unit width over the upper interface of the current, following Cenedese and Adduce [15] and Adduce et al. [2], defined as follows:

$$u_e = \frac{Q_e}{S} = \frac{dV_c}{dt}\frac{1}{S} \tag{4}$$

being Q_e the entrained discharge and S the area of the permeable interface of the current, through which entrainment occurs, both time dependent variables and defined per unit width, being dV_c/dt and S assessed by our experiments. The nature of the gravity currents herein performed is highly unsteady, i.e., their characteristics change continuously as the current evolves towards downstream. In order to evaluate a global entrainment parameter for each run, a bulk evaluation of the properties of the gravity current between two sections was considered. A bulk value for u_e was obtained considering the initial and final configurations of the current during a run for the bulk estimation of dV_c/dt while S was defined at the end of the experiment. In full depth lock-release flows, the return current, propagating above the denser current in the opposite direction, has non-negligible velocity. Therefore, the difference between mean velocities of both denser and return currents, Δu (cf. Table 1), is here considered as the bulk characteristic velocity of the flow (u in Eq. 3). Considering the bulk height of the denser current, $\bar{h}$, as $\bar{h} \approx 1/3h_0$, based on the performed experiments [41] and by mass conservation considerations, the characteristic velocity of the flow results in $\Delta u \approx 1.5u_{f,b}$.

Bulk densimetric Froude and Reynolds numbers were estimated by:

$$Fr_b = \frac{u_{f,b}}{\sqrt{g\Delta\bar{\rho}/\rho_0\bar{h}}}, \tag{5}$$

$$Re_b = \frac{u_{f,b}\bar{h}}{\nu}, \tag{6}$$

where $\Delta\bar{\rho}$ is the mean excess density of the current taking into account the mean density of the current in its initial and final configurations, i.e., in the lock and when the current reached the end of the tank.

Figure 3 shows the entrainment parameter obtained for each run as function of bulk Froude and Reynolds numbers. In general, entrainment parameter, E_b, increases with both Fr_b and Re_b and a plot with a combination of both, Fr_bRe_b clearly shows this relation. Gravity currents performed with higher initial excess density are expected to have higher values of overall entrainment. Regarding the influence of the bed roughness, slight entrainment increase is detected when comparing runs R1 and R2, over rough bed, with run D2, over smooth bed, suggesting that bed roughness induces higher entrainment. This trend, however, is not followed by run R3, where a lower value for E_b is obtained when using sediments with higher roughness scale to compose the channel bed. Apparently, the effect of extra bed drag in run R3 is more effective in the reduction of current velocity rather than promoting higher entrainment of ambient fluid, confirmed by lower Fr_b and Re_b numbers (cf. Table 1).

Keulegan [31] defined a stability parameter for mixing in stratified flows, $\phi = 1/(Fr^2Re)^{1/3}$ (in Vanoni [61]), representing the dependence of mixing on both viscous and gravity forces. This parameter is analogous to Fr_bRe_b (Fig. 3), the difference being attributed to the length scale $\bar{h}$, which is canceled in ϕ. A critical value of the stability parameter for turbulent flows was experimentally obtained by Keulegan [31], $\phi_c = 0.18$, above which no mixing is expected to occur. For comparison purposes, ϕ was herein computed

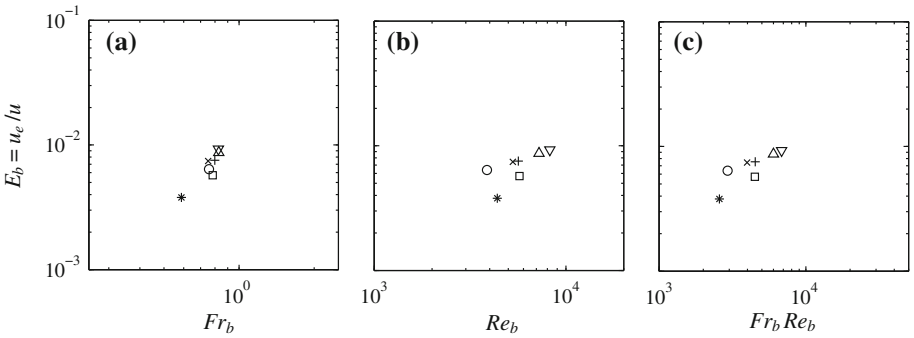

Fig. 3 Entrainment parameter as function of Fr_b (**a**), Re_b (**b**) and $Fr_b Re_b$ (**c**) (symbols explained in Table 1)

with Fr_b and Re_b and was seen to vary in the range $0.06 < \phi < 0.09$, the lowest value being obtained for the run with highest initial excess density, which is also the run where the highest value for the entrainment parameter, E_b, was obtained.

Figure 4 shows the entrainment parameter as function of bulk densimetric Froude number for the present experiments and previous results found in the literature, for gravity currents with $Fr > 0.7$, both from laboratory experiments and field observations. Previous experimental results herein presented concern continuously fed gravity currents developing over smooth sloping beds, in both rotating [15,17,62] and non rotating [4,20] experimental apparatus. Field data was obtained in Lake Ogawara [18], Mediterrean [51], Denmark Strait [24], Faroe Bank Channel [39], Baltic Sea [8] and in atmospheric katabatic flows [52]. Figure 4 also presents well-known entrainment parameterizations proposed by Ellison and Turner [20], for conservative gravity currents, and by Parker et al. [48], based on both conservative and non-conservative currents.

Figure 4 confirms what was observed in Fig. 3 regarding the dependence of the entrainment parameter on Froude number. Significant deviations of the entrainment parameter for the same Froude number are observed. Martin et al. [38] observed a similar behavior when comparing the entrainment coefficient of gravity currents in the field and in the laboratory; entrainment coefficient had significant deviation for the same Richardson number, leading to conclude that it is unreasonable to have a single relationship of the type $E = f(Ri)$ to cover all shear stratified flows. Those deviations are due to the dependence of the entrainment coefficient also on Reynolds number (cf. [15] where is shown that E_b is also an increasing function of Re_b). In Fig. 4, entrainment parameter obtained in katabatic flows [52], with $Re \sim 10^7$, is always higher than values obtained in continuously fed gravity currents in laboratory by Ellison and Turner [20] with $Re \sim 10^3$. It is important to note that entrainment occurs under subcritical conditions ($Fr < 1$), which is supported by oceanic observations, by our experimental results and from Cenedese et al. [17] (cf. Fig. 4) and also confirmed by field data from Fernandez and Imberger [21], Elder and Wunderlich [19] and Hebbert et al. [28].

The entrainment parameter obtained for the performed runs, with kinematics nevertheless different from the gravity currents whose results are shown in Fig. 4, agrees well with previous results, in particular with the entrainment estimations of Cenedese and Adduce [15]. Bed roughness seems to play a role since a clear deviation of run R3, performed with higher roughness scale (cf. Table 1), from the remaining runs is detected. Runs R1 and R2, with lower roughness scale, do not show significant difference from the smooth bed run

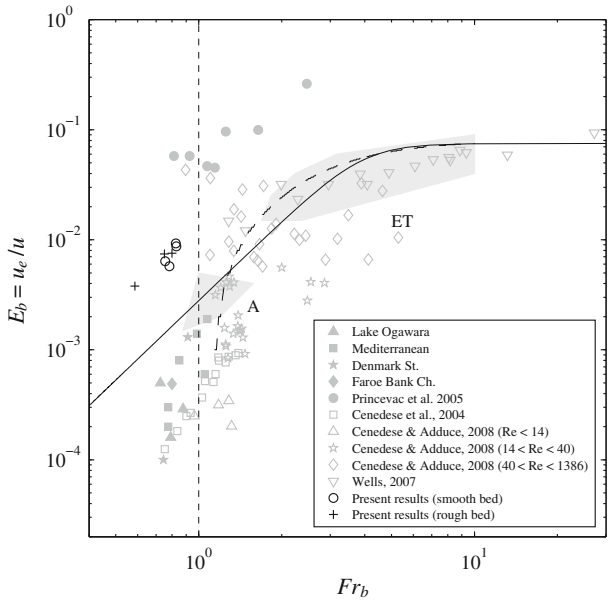

Fig. 4 Entrainment parameter as function of Froude number. Comparison of present results with results obtained in the field (*solid symbols*), in the laboratory (*open symbols and shaded areas* for experiments of Ellison and Turner [20], ET, and Alavian [4], *A*) and entrainment laws suggested by Ellison and Turner [20] (*dashed line*) and Parker et al. [48] (*solid line*) (data from Cenedese and Adduce [15])

D2, with same initial buoyancy, suggesting that the scale of the bed roughness, and possibly porosity, are parameters that influence current kinematics and, therefore, needs further investigation.

3.2 Head dynamics

3.2.1 Head definition

In order to assess local parameters at the current head, a criterion to isolate this region needs to be established. Previous contributions have shown that the head is the region where higher density is observed within the current [25,26,36], which is in accordance with the results herein presented (cf. Fig. 2). Therefore, the criterion used to characterize and isolate this region is based on a dynamic function given by the product between local values of depth-averaged density, $\bar{\rho}_v$, and current height, h:

$$W(x,t) = \bar{\rho}_v(x,t)h(x,t) \tag{7}$$

The downstream limit of the head is given by the position of the foremost point of the current, being the upstream limit, and consequently the head length L_h, defined by taking the position of the first meaningful local minimum of function W, near the front. Figure 5 shows a scheme of the current with the definition of the characteristic variables of the head. The mass of the head of the gravity current per unit width, M_h, is then evaluated by integrating function W over the head length, L_h, given by:

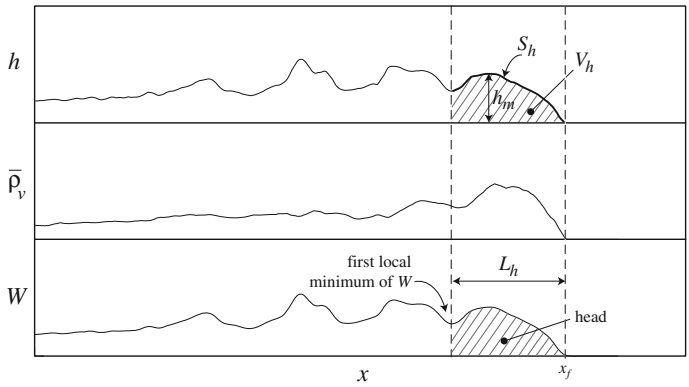

Fig. 5 Definition of the density current head and its characteristic variables: maximum height, h_m, area of the permeable interface per unit width, S_h, volume per unit width, V_h, length, L_h, and front position, x_f

$$M_h(t) = \int_{x_f(t)-L_h(t)}^{x_f(t)} W(x,t)dx \tag{8}$$

where $x_f(t)$ is the position of the foremost point of the current.

3.2.2 Front velocity

The time-varying front velocity of the gravity current, $u_f(t)$, was obtained by derivation in time of the regression functions adjusted to the front position (cf. [41]). Generally, two distinct phases were observed for the development of the current: (i) first phase, or slumping phase, characterized by a linear relation between front position and time after the gate removal and (ii) second phase, or self-similar phase, in which the current moves under the balance between buoyancy and inertial forces, being the front position an evident nonlinear function of time; the transition between both phases was seen to occur at $x_f/x_0 = 9.4 \pm 1.0$, corroborating previous observations [53]. No viscous phase was observed in the performed experiments due to geometric limitations of the experimental tank.

During the slumping phase, the normalized front velocity (by u_0, Eq. 2) was obtained in the range $u_f/u_0 = 0.46 \pm 0.02$, values slightly higher than the predictions of the DNS model by Cantero et al. [14], $u_f/u_0 = 0.42$, and below the theoretical predictions of [9], $u_f/u_0 = 0.527$ for an average current height of $\bar{h}/h_0 = 1/3$. For the self-similar phase, the normalized front velocity was seen to decrease with time as $t^{[-0.19,-0.27]}$, decreasing rates lower than the predictions in literature ($t^{-1/3}$, [14,53]).

Densimetric Froude number based on local variables (discussed in Nogueira et al. [41]), is herein defined as:

$$Fr_h = \frac{u_f}{\sqrt{g\Delta\rho_h/\rho_0 h_m}} \tag{9}$$

where $\Delta\rho_h = \rho_h - \rho_0$, being ρ_h the head-averaged density of the current at each instant and h_m the maximum height of the head (cf. Fig. 5).

During the constant-velocity phase, Fr_h exhibits some scatter which is reduced in the self-similar phase, where a narrow collapse around $Fr_h = 0.9$ is obtained. Run R3 deviates from the general trend, assuming, in general, lower Froude numbers than the remaining runs;

a decreasing trend is observed in the early stages of the current development, evolving towards a plateau of $Fr_h = 0.6$ after $(x_f - x_0)/x_0 = 9$.

At the early stage no apparent head detached from the remaining current is observed and buoyancy effects are given by the total body, thus evolution is governed by the bulk movement of the denser mass stored in the lock. This may explain the scatter in Froude numbers for $(x_f - x_0)/x_0 < 9$, justifying the bulk character of the current propagation at this stage and that local parametrization may not be adequate here. During the second phase, when the reflected bore catches the front of the current (cf. [53]), the current is clearly fragmented into a body and a well defined head with own momentum penetrating in the ambient fluid. The front velocity is determined by this detached head being in equilibrium with its buoyancy celerity. These observations suggest that after the constant-velocity phase current kinematics are ruled by the current head, i.e., the remaining body of the current does not seem to play an important role in the current development.

3.2.3 Head variables

Figure 6 shows the temporal evolution of the head mass per unit width, M_h, plotted as function of dimensionless time, tu_0/x_0, after the gate removal.

Remarkable patterns characterized by successive events of stretching and break of the head are observed (cf. Fig. 6, run D2). Similar behavior was observed when analyzing other variables computed at the head, namely L_h, S_h and V_h, not presented here (cf. [40]). During the stretching phase, a general increase of the head is observed due to entrainment of ambient fluid into the head region. These observations suggest that entrainment at the head is present throughout its development, inclusively in the early stages (in agreement with the observations of Hacker et al. [25], consequently deviating from the theory of Hallworth et al. [26]), where a faster rate of increase of both head length and mass is observed. The break cycles show that a limit exists in the entrainment capacity of the head, indicating an instability process eventually controlled by a dynamical quantity. After this limit is reached, the head breaks leaving behind quasi-steady large-scale billows, which eventually fade in time by diffusion-

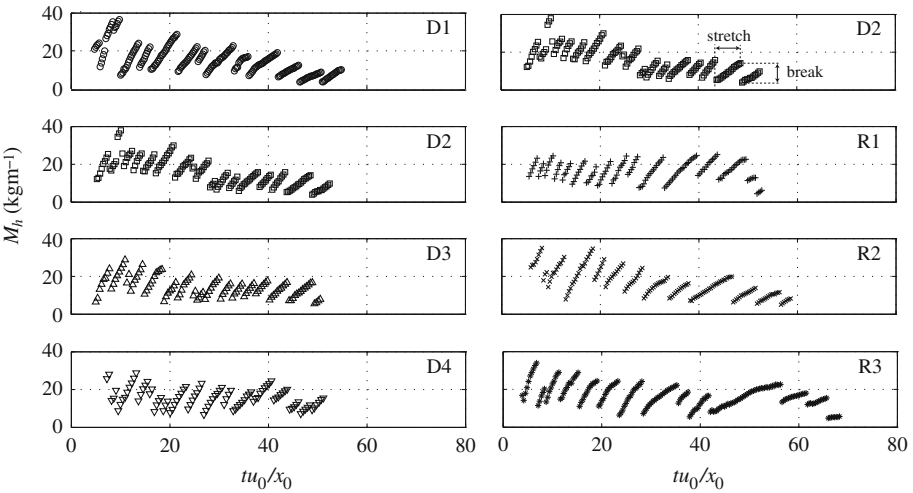

Fig. 6 Mass per unit width of the gravity current head, M_h, as function of non-dimensional time

type processes. This is visible in Fig. 2, following the evolution of the billow structure at positions $(x - x_0)/x_0 = 7.0$, 8.0 and 8.5 (at t =20, 28 and 36 s, respectively). A detailed characterization of the stretching cycles, namely their periodicity and the analysis of the evolution of head variables during stretching, is presented in Sect. 3.4.

3.3 Head entrainment

3.3.1 Entrainment parameterization

Entrainment parameter at the head, E_h, was estimated for each stretching phase (cf. Sect. 3.2.3) by analogy to E_b (Eq. 3), being the initial and final sections considered corresponding to the begin and end of each stretching phase, respectively, leading therefore to one value of E_h for each phase.

Figure 7 shows the entrainment discharge at the head per unit width, $Q_{e,h}$, obtained by computing the variation of volume of the head during each stretching phase, normalized by bulk entrainment discharge earlier estimated, Q_e, as function of non-dimensional time tu_0/x_0. The ratio $Q_{e,h}/Q_e$ shows that entrainment discharge at the head is significantly higher than its bulk estimation for the entire current. In general, the entrained discharge decreases in time as expected given the results presented in Fig. 6, where it is shown that the slope of M_h in each stretching phase tends to decrease in time. In the early stages of current development, i.e., for $tu_0/x_0 < 20$ approximately, the ratio $Q_{e,h}/Q_e$ is, in average, $Q_{e,h}/Q_e \approx 3$, thereafter it decreases linearly, until $tu_0/x_0 = 40$, converging to $Q_{e,h}/Q_e = 1$. For later instants, the ratio remains approximately constant and equal to 1. A good data collapse between runs is observed except for run R3, which shows, in average, a ratio $Q_{e,h}/Q_e$ twice the value for the remaining runs during most part of the current development, converging nevertheless to $Q_{e,h}/Q_e = 1$ for $tu_0/x_0 > 40$.

The entrainment velocity, $u_{e,h}$, was computed in analogy to Eq. 4, considering the entrained discharge over the permeable surface of the head, S_h, averaged over each stretching phase, and is presented in Fig. 8 normalized by bulk entrainment velocity earlier estimated, u_e. The ratio $u_{e,h}/u_e$ shows that the entrainment velocity at the head is much higher

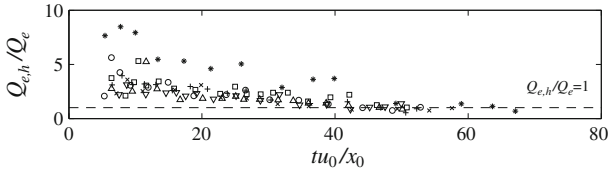

Fig. 7 Entrainment discharge at the head normalized by bulk entrainment discharge as function of non-dimensional time, one value per stretching phase (symbols explained in Table 1)

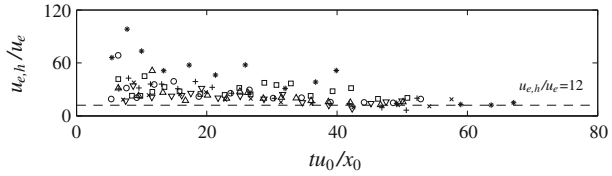

Fig. 8 Local entrainment velocity normalized by bulk entrainment velocity as function of non-dimensional time, one value per stretching phase (symbols explained in Table 1)

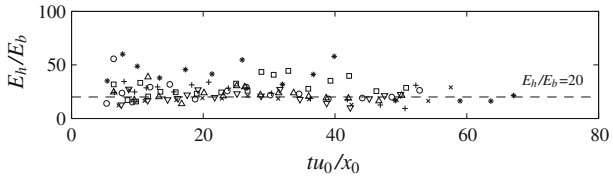

Fig. 9 Entrainment parameter at the head normalized by bulk entrainment parameter as function of non-dimensional time, one value per stretching phase (symbols explained in Table 1)

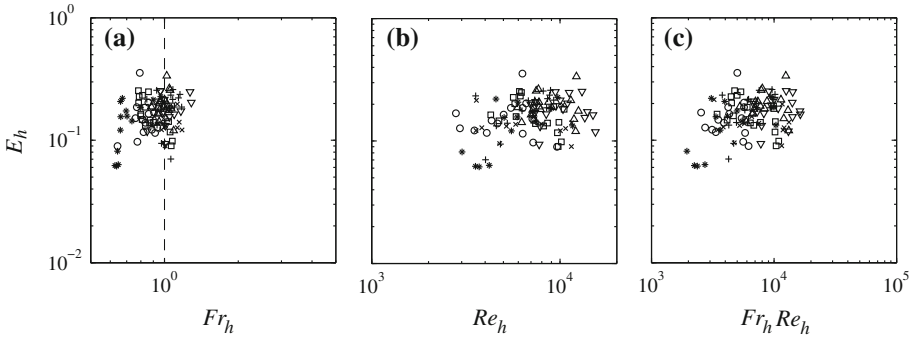

Fig. 10 Entrainment parameter at the head as function of Fr_h (**a**), Re_h (**b**) and $Fr_h Re_h$ (**c**) (symbols explained in Table 1)

than the bulk entrainment velocity u_e, being in average $u_{e,h} \approx 30u_e$ in the beginning of a run, reducing to $u_{e,h} \approx 12u_e$ at the end. The entrainment velocity follows the same trend of $Q_{e,h}$, generally decreasing over time. Again, run R3 stands out, showing a ratio of twice that of the remaining runs, nevertheless converging to $u_{e,h} \approx 12u_e$ as the experiment continues.

Figure 9 presents the entrainment parameter estimated at the head normalized by bulk entrainment parameter, E_b. The ratio E_h/E_b shows an approximately constant trend over time, oscillating around $E_h/E_b \approx 20$ with some significant scatter. Values of this ratio corroborate what was observed previously in Figs. 7 and 8, allowing the conclusion that entrainment at the head is more intense than in the current as a whole.

On Fig. 10, E_h versus densimetric Froude and Reynolds numbers computed at the head of the current are plotted. Local densimetric Froude number, Fr_h, was computed by Eq. 9 and local Reynolds number, Re_h, was assessed through $Re_h = u_f h_m/\nu$, being subsequently averaged within each stretching phase. Densimetric Froude number show that the head region develops under critical flow conditions since data is distributed in a cloud around $Fr \approx 1$. Figure 10(b,c) shows that, although the main tendency is to have an increase of entrainment with increase of Re_b and $Fr_b Re_b$, no clear dependence of E_h on Re_h or $Fr_h Re_h$ seems to exist.

3.3.2 Mass rate

As shown in Fig. 6, the mass of the gravity current head grows during each stretching phase due to entrainment of ambient fluid into this region, until it reaches a limit and breaks, from where it starts expanding again. The mass growing rate, or stretching rate, of the head can be analyzed by computing the variation of mass during each stretching event over time,

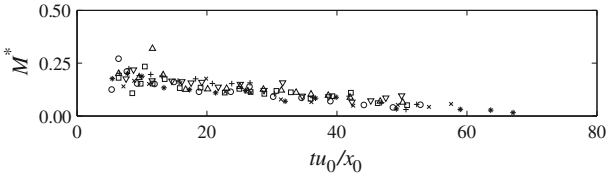

Fig. 11 Non-dimensional mass rate as function of non-dimensional time (symbols explained in Table 1)

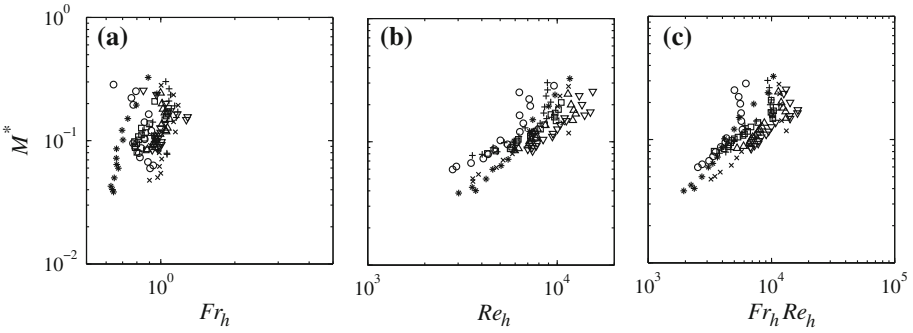

Fig. 12 Non-dimensional mass rate as function of Fr_h (**a**), Re_h (**b**) and $Fr_h Re_h$ (**c**) (symbols explained in Table 1)

i.e., dM_h/dt, herein taken as a measure to assess the entrainment rate at the head. This quantity is here normalized by the initial mass in the lock, M_0, resulting the parameter $M^* = dM_h/dt M_0^{-1}$. Time derivative was computed through application of second order centered finite differences to the experimental data $M_h(t)$, after applying a moving average ($N = 10$) to instantaneous data. Figure 11 shows the average of M^* over non-dimensional time, tu_0/x_0, for each stretching phase, for all runs.

In general, the mass growing rate decreases as the current advances, suggesting that the entrainment rate at the head is ruled by local reduced gravity. As the current develops and ambient fluid is entrained into the current head, local reduced gravity, the driving force of the current, is reduced due to current dilution and, consequently, current decelerates leading to less fluid to be entrained at the current head. Figure 11 shows mass growing rates with a similar decaying trend between runs and their collapse suggests that temporal variation of mass inside the head poorly depends on initial density in the lock ρ_1 and bed roughness k_s. In the authors opinion, the mass growing rate should tend to an equilibrium state (i.e. $M^* = 0$), not seen in these experiments due to geometric limitations of the experimental apparatus.

On Fig. 12 the dependence of M^* on local densimetric Froude and Reynolds numbers, Fr_h and Re_h respectively, averaged over each stretching phase, is presented. In general, the dependence on Fr_h is not clear, except for run R3 where it exhibits an increasing trend with Fr_h. Densimetric Froude numbers oscillate around $Fr \approx 1$, suggesting that the head develops under critical conditions. On the other hand, M^* is an increasing function of Re_h. This results from the continuously decreasing trend of Re_h over time together with M^*. For high values of Re_h, M^* increases significantly, showing that mass transfer between current and ambient fluid due to turbulent phenomena is more effective than due to viscous effects, during the initial stages of the current development. For lower values of Re_h, there is a linear relation between M^* and Re_h. When plotting Fr_h and Re_h together, $Fr_h Re_h$, the linear dependence of M^* on $Fr_h Re_h$, for lower values of the latter, becomes evident. This is due

to the effect of the local reduced gravity, $g\Delta\rho_h/\rho_0$, which highlights the similarity between runs. That linear phase corresponds to the final stages of the current development, where Re_h, M^* and Fr_h (although Fr_h not consistently), decrease. Fig. 12(b,c) shows that for high values of Re_h and $Fr_h Re_h$ the dependence on Re_h seems to vanish, which is typical behavior of fully developed turbulent flows.

3.4 Stretching characterization

Figure 13 presents the temporal evolution of the mass of the gravity current head normalized by the initial mass in the lock, M_h/M_0, and plotted as a function of dimensionless front position $(x_f - x_0)/x_0$. Although the information is somewhat analogous to the one presented in Fig. 6, the use of the of dimensionless front position highlights the similarity in the stretching events between runs. In general, limits of growth of M_h/M_0 are more or less constant during the first phase of the current development when buoyancy overcomes inertial effects, i.e., for $(x - x_0)/x_0 < 9$ it varies approximately in the range limited by $0.2 < M_h/M_0 < 1$, which means that the head tends to break when its mass reaches a value of the same order of that initially in the lock. During the second phase, i.e., for $(x - x_0)/x_0 > 9$, the ratio M/M_0 tends to decrease as the current evolves.

In order to analyze the periodicity of the breaking events, Table 2 presents the average and maximum non-dimensional wave length, $\mathcal{L}^* = \mathcal{L}/x_0$, where $\mathcal{L}$ is the spatial distance between front positions of two successive breaking events and the average and maximum non-dimensional period between breaking events, $T^* = Tu_0/x_0$, being T the time between two successive breaks.

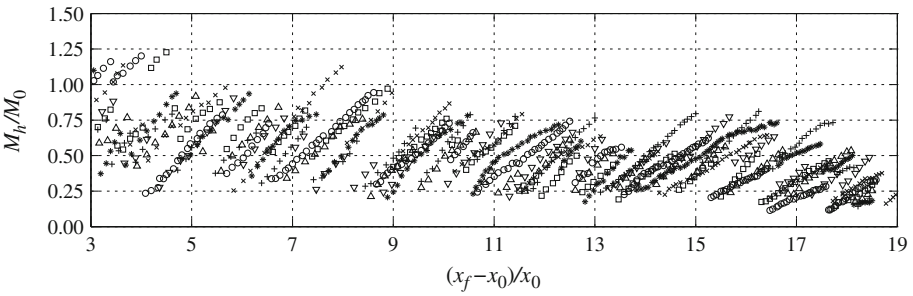

Fig. 13 Non-dimensional mass per unit width of the gravity current head, M_h/M_0, as function of non-dimensional front position (symbols explained in Table 1)

Table 2 Average and maximum normalized temporal (T) and spatial ($\mathcal{L}$) periodicity of breaking events

Run	$\overline{T^*}$	T^*_{max}	$\overline{\mathcal{L}^*}$	$\mathcal{L}^*_{max}$
D1	3.3	5.9	1.1	2.0
D2	2.5	5.2	0.9	1.5
D3	2.7	5.5	0.9	1.8
D4	2.6	4.2	0.9	1.6
R1	3.0	6.8	1.0	2.0
R2	4.1	8.8	1.3	2.3
R3	4.6	14.4	1.2	2.9

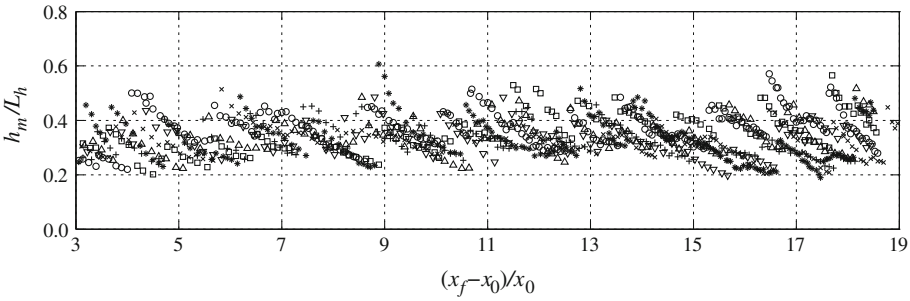

Fig. 14 Head aspect ratio, h_m/L_h, as function of non-dimensional front position (symbols explained in Table 1)

The average wave length is approximately constant between runs, $\mathcal{L}^* = 1.1 \pm 0.2$ (cf. Table 2), which is depicted by the similarity in the plots of Fig. 13. The maximum wave length shows an increasing trend with bed roughness. The period of the breaking events, T^*, is quite irregular within a run (cf. Fig. 6), where no consistent evolution trend is identified. However, the analysis of the average and maximum values of T^* show a tendency between runs (cf. Table 2). Regarding the effect of the initial density for smooth bed (runs D1, D2, D3 and D4), we observe that run D1, with lower initial density, has the highest average and maximum stretching periods. A significant decrease in the average periodicity is observed from run D1 to D2, which apparently stabilizes with the following increase of initial density. The effect of bed roughness can be observed by analyzing the sequence D2, R1, R2 and R3. The average period suggests that as the bed roughness increases, breaking events tend to occur less frequently and a temporal extension of the stretching phases occurs. A similar trend is observed when looking to the maximum period between breaking events; a remarkable increase in the maximum period (5.2, 6.8, 8.8, 14.4) is detected when increasing the bed roughness, trend also observed in the analysis of the maximum wave length $\mathcal{L}^*$.

The aspect ratio of height versus length, h_m/L_h, is plotted in Fig. 14 for all runs. The aspect ratio of the head is seen to decrease during the stretching period, which is expected since the maximum height of the head has little variation over time while the head length increases continuously during stretching. However, there is a limit in the entrainment capacity of the head, shown by the breaks at $h_m/L_h \approx 0.2$. Britter and Linden [11] suggested that the head aspect ratio of constant-flux gravity currents developing over horizontal beds is zero, as shown by Fig. 8 therein. Nevertheless, the fit line presented for h/L_h as function of slope, based on results from their own experiments and previous ones, clearly indicates a trend towards 0.2 as the slope angle approaches zero. Özgökmen [46] presents a limit of $h/L_h = 0.2$, for numerical modeling in lock-exchange gravity currents down slope (3.5°), being 0.25 their average or trend. Hence, the limit given by the head aspect ratio, $h_m/L_h = 0.2$, is essentially a good criterion to predict the instant of head breaking, for unsteady currents developing over horizontal beds, or even, over small slopes.

To evaluate the similarity within stretching periods, a phase analysis is performed over one cycle of duration θ, varying from 0 to 1, where 0 is the begin and 1 the end of the stretching cycle. The collapse of the stretching cycles of the variables h_m/L_h, M_h/M_0, E_h/E_b and M^* were analyzed by plotting all cycles together, for each variable and for each run. A very good data collapse is observed, highlighting the similarity between stretching cycles for the variables under analysis. For comparison between runs, the phase average trend of each

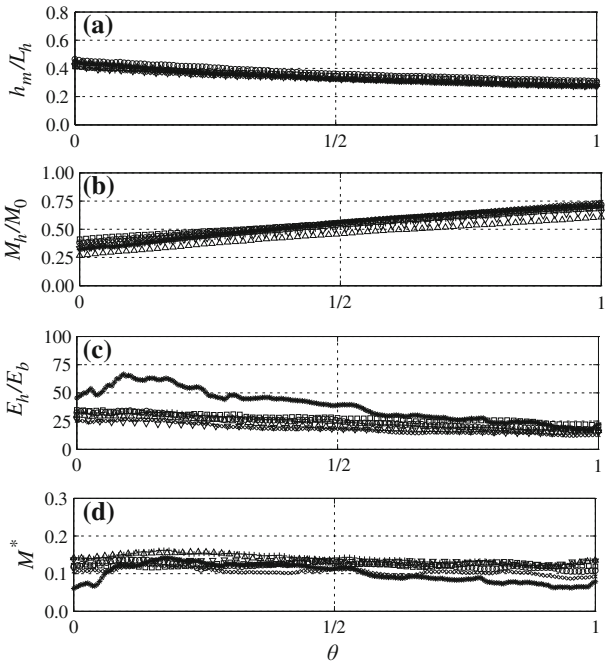

Fig. 15 Phase-averaged variables as function of the duration of a stretching cycle, θ: **a** head aspect ratio, h_m/L_h, **b** non-dimensional head mass, M_h/M_0, **c** entrainment parameter at the head over global entrainment parameter, E_h/E_b, and **d** non-dimensional mass growing rate, M^* (symbols explained in Table 1)

variable is analyzed. Given the different number of points in each stretching cycle, a sub-discretization of data over one cycle was adopted, taken the shortest temporal discretization within each run, which corresponds to the discretization of the stretching cycle with more data points. Then, values of variables under analysis are interpolated linearly in order to have one data point for each additional instant, being then possible to compute phase averages for each run.

Figure 15 shows phase-averaged values so obtained over each cycle of variables h_m/L_h, M_h/M_0, E_h/E_b and M^*. As already observed in the ensemble plots of the non-dimensional mass and of the head aspect ratio (Figs. 13 and 14, respectively), a high similarity of these variables between stretching cycles do exist which is highlighted in Fig. 15a,b. In average terms, the limit attained by the head aspect ratio, related to the end of the stretching phase/occurrence of break event, is around $h_m/L_h \approx 0.3$, corroborating previous experimental and numerical findings. Mean non-dimensional head mass vary in average between $0.25 < M_h/M_0 < 0.75$. The ratio of local over global entrainment parameters, E_h/E_b (Fig. 15c), also shows a good similarity between runs, clarifying the average trend around $E_h \approx 20E_b$, as already suggested in Sect. 3.3. Also the deviation of run R3 becomes rather clear, approaching the overall trend of the remaining runs in the final stages of stretching. Finally, the evolution of M^* (Fig. 15d) during stretching is seen to vary little. There is a general slight increase during the first half of the standard stretching duration, followed by a decrease during the second half. Run R3 exhibits this trend as well, although with a higher amplitude than the remaining runs.

4 Conclusions

An image analysis technique was used to investigate the dynamics of the head of lock-released gravity currents developing over smooth and rough beds. The influence of the initial buoyancy of the gravity current on its development was assessed, as well as the influence of bed roughness.

Immediately after the release of the dense fluid inside the lock, a gravity current of heavy fluid forms near the bed and evolves towards downstream. During its development, the current mixes with the surrounding ambient fluid and continuously entrains part of it. The interaction between fluids is more dynamic in the head region and a notorious pattern of head stretching and break was herein observed. As the head entrains ambient fluid, its dimensions and mass increase accordingly, until it becomes unstable and, consequently, breaks. After breaking, the head leaves behind quasi-steady large-scale billows that remain at the rear of the head, promoting strong mixing in that region, which eventually fade in time by diffusion-type processes. The evolution of the head aspect ratio during the stretching period shows a consistent limit, for all performed runs, of $h_m/L_h = 0.2$, corresponding to the breaking instants. In addition, during these instants the mass of the gravity current head is seen to be of the same order of the mass initially in the lock, especially during the first phase of the current development. Bed roughness is seen to play an important role in this process. As roughness increases, besides the expected current deceleration, the break events become less frequent. Similarity of the stretching events between runs is confirmed by the consistent collapse of the analyzed variables at the head.

The bulk entrainment parameter obtained for each run shows that entrainment occurs under subcritical conditions and its magnitude is in good agreement with entrainment predictions of Cenedese and Adduce [15]. Gravity currents with higher initial density are expected to have higher values of entrainment parameter. Regarding the influence of the bed roughness, only the run performed with higher roughness shows a clear deviation from the remaining runs, suggesting that roughness scale and porosity might play a role in the gravity current dynamics. The dependence on Froude and Reynolds numbers was also confirmed by our experiments. Entrainment parameter at the head was assessed for each stretching phase and was seen to be approximately 20 times higher the entrainment parameter obtained in a bulk fashion for the entire current.

The evolution of the mass growing rate at the head shows a decreasing trend in time, suggesting that local buoyancy rules the entrainment phenomenon. The entrained ambient fluid reduces the driving force of the current, due to current dilution, leading to less fluid to be entrained at the current head. Its similarity between runs suggests that this parameter is independent from the initial density gradient and the bed roughness. Both Froude and Reynolds numbers influence, naturally, the evolution of the mass growing rate. In particular, a linear increasing relation is observed for lower values of $Fr_h Re_h$, corresponding to later stages of the current development, when all the parameters in question decrease consistently. For high Reynolds numbers, entrainment increases significantly indicating a higher efficiency of turbulent-type processes in entraining ambient fluid when compared to viscous diffusion. The results presented herein indicate that entrainment at the head is present in gravity currents with densimetric Froude numbers below 0.7 and it was observed at all stages of the current development, including the early stages, where higher entrainment rates are observed.

Acknowledgments This research was supported by the European Fund for Economic and Regional Development (FEDER) through the Program Operational Factors of Competitiveness (COMPETE) and National Funds through the Portuguese Foundation for Science and Technology (FCT) with the research project

PTDC/ECM/099752/2008, FCOMP 01 0124 FEDER 009735 and the research grant SFRH/BD/48705/2008. Acknowledgments are due to Alexandre Sousa for helping in data interpretations. The authors would like to thank the reviewers for the comments and suggestions that certainly improved the content of the manuscript.

References

1. Adduce C, Lombardi V, Sciortino G, Morganti M (2009) Roughness effects on gravity currents dynamics. In: Proceedings of 33rd IAHR congress, Vancouver, Canada
2. Adduce C, Sciortino G, Proietti S (2012) Gravity currents produced by lock-exchanges: experiments and simulations with a two layer shallow-water model with entrainment. J Hydr Eng 138(2):111–121
3. Alahyari A, Longmire EK (1996) Development and structure of a gravity current head. Exp Fluids 20:410–416
4. Alavian V (1986) Behaviour of density currents on an incline. J Hydr Eng 112(1):27–42
5. Allen JRL (1971) Mixing at turbidity currents heads, and its geological implications. Sediment Petrol 41(1):97–113
6. Altinakar MS (1993) Weakly depositing turbidity currents on small slopes. PhD thesis, École Polytechnique Fédérale de Lausanne (EPFL), Lausanne, Switzerland
7. Alves E, González J, Freire P, Cardoso H (2008) Experimental study of plunging turbidity currents in reservoirs. In: Proceedings of river flow 2008, Çeşme-Izmir, Turkey
8. Arneborg L, Fiekas V, Umlauf L, Burchard H (2007) Gravity current dynamics and entrainment—a process study based on observations in the Arkona Basin. J Phys Oceanogr 37:2094–2113
9. Benjamin TB (1968) Gravity currents and related phenomena. J Fluid Mech 31:209–248
10. Bombardelli FA, Cantero MI, García MH, Buscaglia GC (2009) Numerical aspects of the simulation of descontinuous saline underflows: the lock-exchange problem. J Hydr Res 47(6):777–789
11. Britter RE, Linden PF (1980) The motion of the front of a gravity current travelling down an incline. J Fluid Mech 99(3):531–543
12. Britter RE, Simpson J (1978) Experiments on the dynamics of a gravity current head. J Fluid Mech 88(2):223–240
13. Cantero MI, Lee JR, Balachandar S, García MH (2007) On the front velocity of gravity currents. J Fluid Mech 586:1–39
14. Cantero MI, Balachandar S, García MH, Bock D (2008) Turbulent structures in planar gravity currents and their influence on the flow dynamics. J Geophys Res 113 (C08018)
15. Cenedese C, Adduce C (2008) Mixing in a density driven current flowing down a slope in a rotating fluid. J Fluid Mech 604:369–388
16. Cenedese C, Adduce C (2010) A new entrainment parametrization for mixing in overflows. J Phys Oceanogr 40(8):1835–1850
17. Cenedese C, Whitehead JA, Ascarelli TA, Ohiwa M (2004) A dense current flowing down a sloping bottom in a rotating fluid. J Phys Oceanogr 34:188–203
18. Dallimore CJ, Imberger J, Ishikawa T (2001) Entrainment and turbulence in saline underflow in Lake Ogawara. J Hydr Eng 127(11):937–948
19. Elder RA, Wunderlich WO (1972) Inflow density currents in TVA reservoirs. In: Proceedings of international symposium on stratified flows, Novosibirsk, Russia
20. Ellison TH, Turner JS (1959) Turbulent entrainment in stratified flows. J Fluid Mech 6:423–448
21. Fernandez RL, Imberger J (2006) Bed roughness induced entrainments in a high Richardson number underflow. J Hydr Res 44(6):725–738
22. García MH, Parsons JD (1996) Mixing at the front of gravity currents. Dyn Atmospheres Oceans 24:197–205
23. Gerber G, Diedericks G, Basson GR (2011) Particle image velocimetry measurements and numerical modeling of a saline density current. J Hydr Eng 137(3):333–342
24. Girton JB, Sanford TB (2003) Descent and modification of the overflow plume in Denmark Strait. J Phys Oceanogr 33:1351–1364
25. Hacker J, Linden PF, Dalziel SB (1996) Mixing in lock-release gravity currents. Dyn Atmospheres Oceans 24:183–195
26. Hallworth MA, Huppert HE, Phillips JC, Sparks RSJ (1996) Entrainment into two-dimensional and axisymmetric turbulent gravity currents. J Fluid Mech 308:289–311
27. Härtel C, Meiburg E, Necker F (2000) Analysis and direct numerical simulation of the flow at a gravity-current head. Part 1. Flow topology and front speed for slip and no-slip boundaries. J Fluid Mech 418:189–212

28. Hebbert B, Imberger J, Loh I, Patterson J (1979) Collie River underflow into the Wellington reservoir. J Hydr Div ASCE 105(5):533–545
29. Huppert HE, Simpson JE (1980) The slumping of gravity currents. J Fluid Mech 99(4):785–799
30. Kestin J, Khalifa HE, Correia RJ (1981) Tables of the dynamic and kinematic viscosity of aqueous NaCl solutions in the temperature range 20-150c and the pressure range 0.1-35 MPa. Phys Chem Ref Data 10(1):71–87
31. Keulegan GH (1949) Interfacial instability and mixing in stratified flows. J Res US Bur Stand 43:487–500
32. Khavasi E, Afshin H, Firoozabadi B (2012) Effect of selected parameters on the depositional behaviour of turbidity currents. J Hydr Res 50(1):60–69
33. La Rocca M, Adduce C, Sciortino G, Pinzon AB (2008) Experimental and numerical simulation of three-dimensional gravity currents on smooth and rough bottom. Physics Fluids 20
34. La Rocca M, Adduce C, Lombardi V, Sciortino G, Hinkelmann R (2012a) Development of a lattice Boltzmann method for two-layered shallow-water flow. Int J Numer Meth Fluids 70(8)
35. La Rocca M, Adduce C, Sciortino G, Pinzon AB, Boniforti MA (2012b) A two-layer, shalow water model for 3D gravity currents. J Hydr Res 50(2):208–217
36. Marino BM, Thomas LP, Linden PF (2005) The front condition for gravity currents. J Fluid Mech 536:49–78
37. Martin JE, García MH (2009) Combined PIV/PLIF measurements of a steady density current front. Exp Fluids 46:265–276
38. Martin JE, Sun T, García MH (2012) Optical methods in the laboratory: an application to density currents over bedforms. In: Rodi W, Uhlman M (eds) Environmental fluid mechanics: memorial volume in honour of Prof. Gerhard H. Jirka—IAHR Monograph. CRC Press, Taylor & Francis Group
39. Mauritzen C, Price J, Sanford T, Torres D (2005) Circulation and mixing in the faroese channels. Deep-Sea Res I 52:883–913
40. Nogueira HIS, Adduce C, Alves E, Franca MJ (2012) The influence of bed roughness on the dynamics of gravity currents. In: Proceedings of river flow 2012. San José, Costa Rica
41. Nogueira HIS, Adduce C, Alves E, Franca MJ (2013a) Analysis of lock-exchange gravity currents over smooth and rough beds. J Hydr Res 1–15
42. Nogueira HIS, Adduce C, Alves E, Franca MJ (2013b) Image analysis technique applied to lock-exchange gravity currents. Meas Sci Technol 24(047001), 4 pp
43. Oehy C, Schleiss AJ (2007) Control of turbidity currents in reservoirs by solid and permeable obstacles. J Hydr Eng 133(6):637–648
44. Ooi SK, Constantinescu G, Weber LJ (2007) 2D large-eddy simulation of lock exchange gravity current flows at high grashof numbers. J Hydr Eng 133(9):1037–1047
45. Özgökmen TM, Fischer PF (2008) On the role of bottom roughness in overflows. Ocean Model 20(9):336–361
46. Özgökmen TM, Fischer PF, Duan J, Iliescu T (2004) Three-dimensional turbulent bottom density currents from a high-order nonhydrostatic spectral element model. J Phys Oceanogr 34:2006–2026
47. Paik J, Eghbalzadeh A, Sotiropoulos F (2009) Three-dimensional unsteady rans modelling of discontinuous gravity currents in rectangular domains. J Hydr Eng 135(6):505–521
48. Parker G, García MH, Fukushima Y (1987) Experiments in turbidity currents over an erodible bed. J Hydr Res 25:123–147
49. Parsons JD, García MH (1998) Similarity of gravity current fronts. Phys Fluids 10(12):3209–3213
50. Peters WD, Venart JES (2000) Visualization of rough-surface gravity current flows using laser-induced fluorescence. In: Proceedings of 9th international symposium of flow visualization, Edinburgh, Scotland
51. Price JF, Baringer MO (1994) Outflows and deep water production by marginal seas. Prog Oceanogr 33:161–200
52. Princevac M, Fernando HJS, Whiteman CD (2005) Turbulent entrainment into natural gravity-driven flows. J Fluid Mech 533:259–268
53. Rottman JW, Simpson JE (1983) Gravity currents produced by instantaneous releases of a heavy fluid in a rectangular channel. J Fluid Mech 135:95–110
54. Shin JO, Dalziel BS, Linden PF (2004) Gravity currents produced by lock exchange. J Fluid Mech 521:1–34
55. Simpson J (1972) Effects of the lower boundary on the head of a gravity current. J Fluid Mech 53(4):759–768
56. Simpson JE (1997) Gravity currents: in the environment and the laboratory, 2nd edn. Cambridge University Press, New York
57. Simpson J, Britter RE (1979) The dynamics of the head of a gravity current advancing over a horizontal surface. J Fluid Mech 93(3):477–495

58. Thomas LP, Dalziel SB, Marino BM (2003) The structure of the head of an inertial gravity current determined by particle-tracking velocimetry. Exp Fluids 34:708–716
59. Tokyay T, Mohamed YA, Constantinescu G (2011) Effect of Reynolds number on the propagation of the lock exchange gravity currents in a porous medium. In: Proceedings of 34th IAHR congress, Brisbane, Australia
60. Ungarish M, Zemach T (2005) On the slumping of high Reynolds number gravity currents in two-dimensional and axisymmetric configurations. Eur J Mech B/Fluids 24:71–90
61. Vanoni VA (ed) (1975) Sedimentation engineering, manuals and reports on engineering practice no. 54. American Society of Civil Engineers, New York
62. Wells MG (2007) Influence of Coriolis forces on turbidity currents and their sediment patterns. Proceedings of Euromech colloquium
63. Zhu JB, Lee CB, Chen GQ, Lee JHW (2006) PIV observation of instantaneous velocity structure of lock release gravity currents in the slumping phase. Commun Nonlinear Sci Numer Simul 11:262–270